Electrical Contact between an Ultrathin Topological Dirac Semimetal and a Two-Dimensional Material

Liemao Cao,[1,2] Guanghui Zhou,[3] Qingyun Wu,[1] Shengyuan A. Yang,[1] Hui Ying Yang,[4] Yee Sin Ang,[1,*] and L.K. Ang[1,†]

[1] *Science, Mathematics and Technology, Singapore University of Technology and Design, 8 Somapah Road, Singapore 487372, Singapore*

[2] *College of Physics and Electronic Engineering, Hengyang Normal University, Hengyang, 421002, China*

[3] *Department of Physics, Key Laboratory for Low-Dimensional Structures and Quantum Manipulation (Ministry of Education), and Synergetic Innovation Center for Quantum Effects and Applications of Hunan, Hunan Normal University, Changsha, 410081, China*

[4] *Engineering Product Development, Singapore University of Technology and Design, 8 Somapah Road, Singapore 487372, Singapore*

(Received 3 March 2020; revised manuscript received 11 March 2020; accepted 21 April 2020; published 12 May 2020)

Ultrathin films of the topological Dirac semimetal Na_3Bi have recently been revealed as unusual electronic materials with field-tunable topological phases. Here we investigate the electronic and transport properties of ultrathin Na_3Bi as an electrical contact to a two-dimensional (2D) metal (i.e., graphene) and 2D semiconductors (i.e., MoS_2 and WS_2 monolayers). Using combined first-principles density-functional theory and nonequilibrium Green's function simulation, we show that the electrical coupling between bilayer-Na_3Bi thin film and graphene results in a notable interlayer charge transfer, thus inducing sizable n-type doping in the Na_3Bi/graphene heterostructures. In the case of MoS_2 and WS_2 monolayers, the lateral Schottky transport barrier is significantly lower than for many commonly studied bulk metals, thus revealing bilayer Na_3Bi to be a high-efficiency electrical contact material for 2D semiconductors. These findings open up an avenue for utilizing topological semimetal thin film as an electrical contact to 2D materials, and further expand the family of 2D heterostructure devices into the realm of topological materials.

DOI: 10.1103/PhysRevApplied.13.054030

I. INTRODUCTION

Two-dimensional (2D) layered materials and topological semimetals are two of the most-active research fields of current condensed-matter physics, materials science, and applied device engineering. The ever-expanding family of 2D materials, such as graphene [1], transition metal-dichalcogenides (TMDCs) [2], black phosphorus [3], group-VI Xenes [4], MXenes [5], and ferromagnetic $Cr_2Ge_2Te_6$ and Fe_3GeTe_2 [6,7], is widely regarded as a material class of key importance in electronic [8], photonic [9], optoelectronic [10], energetic [11], spintronic [12], and valleytronic [13,14] devices with strong potential in revolutionizing the next-generation solid-state technology. Electrically contacting 2D materials with a metal, however, remains one of the major bottlenecks for the realization of high-performance industrial-grade electronic devices. Although having Ohmic contact is more desirable in reducing power dissipation [15–17], most 2D semiconductors are inevitably plagued by the formation of Schottky contacts with inherently large contact resistance when contacted by a bulk metal [18–21]. Achieving high-quality electrical contact to 2D materials remains an ongoing quest that is critically important for the development of industrial-grade 2D-material-based devices [22,23].

On the other hand, three-dimensional (3D) topological semimetals [24–26] that host exotic topologically protected band crossing in the bulk and topological surface states are another emerging condensed-matter system. For example, 3D topological Dirac semimetals, such as Cd_3As_2 and Na_3Bi [27,28], which host a pair of 3D massless Dirac quasiparticles, have attracted considerable interest in the experimental and theoretical communities [29–31]. The unusual physical properties of topological semimetals has led to myriad unusual physical properties, such as chiral anomaly [30], linear quantum magnetoresistance [32,33], oscillating quantum spin Hall effect [34], charge-carrier mobility exceeding 6000 $cm^2\ V^{-1}\ s^{-1}$ [35], logarithmically diverging giant diamagnetism at the Dirac nodal point [36,37], gate-tunable surface states [38],

*yeesin_ang@sutd.edu.sg
†ricky_ang@sutd.edu.sg

 © 2020 American Physical Society

and strong optical nonlinearity [39]. Intriguingly, Na_3Bi becomes a topological insulator with a band gap of approximately 300 meV in the ultrathin limit of a few atomic layers [40], in which the band structure can be tuned between a topological insulator and a band insulator via an external electric field [41]. The experimental demonstration of a field-effect-tunable topological phase transition in bilayer Na_3Bi [40] thus opens up the possibility of topological nanodevices in which the charge conduction is controlled by the field-effect modulation of the band topology of the transport channel.

Although both 2D materials and 3D topological semimetals have been extensively studied, the union of topological Dirac semimetals and 2D material in terms of contact engineering remains largely unknown thus far. In this work, we explore the integration of topological semimetal ultrathin film into the design of 2D-material-based electronic devices. We propose a concept of utilizing ultrathin films of topological semimetals as an electrical contact to 2D materials. Using a field-effect-transistor setup, we show that the Schottky-barrier height formed at the bilayer Na_3Bi/2D semiconductor is markedly lower than that formed by many bulk metals (see Fig. 6), thus unrevealing the potential of Na_3Bi ultrathin film as an efficient electrode contact to 2D semiconductors. Furthermore, unlike many bulk metals that metalize the 2D semiconductor during contact formation, the electronic band structures of MoS_2 and WS_2 remain intact when contacted by Na_3Bi, thus offering a useful platform for studies of optical, valley, and excitonic physics in 2D TMDCs [42,43]. Importantly, ultrathin Na_3Bi undergoes a metal-to-insulator transition and a topological phase transition from a trivial band insulator to a topological insulator with conducting edge states when it is subjected to an external gate voltage [40,41]. Such gate-tunable electronic properties may be further harnessed as a control for the design of electronic devices. Our findings will open up an avenue toward sub-10-nm-device technology via the union of 2D materials and ultrathin films of 3D topological materials, and further expands the family of 2D-material-based heterostructure devices into the realm of quantum materials with nontrivial topological phases.

II. COMPUTATIONAL METHODS

We perform a first-principles density-functional-theory (DFT) simulation as implemented in the VASP code [44,45] to study the contact between ultrathin bilayer Na_3Bi and (i) semimetallic graphene and (ii) semiconducting MoS_2 and WS_2 monolayers. The geometric optimization and electronic properties of the heterostructures are calculated via DFT simulation as implemented in the VASP code [44,45]. The calculation uses the projector-augmented-wave pseudopotential [46]. During the structure relaxations, spin-orbit coupling (SOC) is not included. SOC is included in the electronic structure calculations. The cutoff energy is set to 500 eV. A vacuum layer of 30 Å in the vertical direction is chosen to avoid interaction between the top and bottom surfaces. Monkhorst-Pack *k*-point sampling is set to be $11 \times 11 \times 1$. The method of Grimme (DFT-D3) for the van der Waals (vdW) interaction functional is used in the calculations [47], and the dipole correction is also added. The residual force is converged to less than 0.01 eV/Å, and the convergence criterion for the total energy is set to be 10^{-6} eV. In addition, the transport properties for the two-probe systems are calculated with use of the Atomistix ToolKit 2018 package based on DFT combined with the nonequilibrum Green's functions [48–51]. SOC is also included in the transport simulation.

III. RESULTS AND DISCUSSION

A. Bilayer-Na_3Bi/graphene heterostructure

Figures 1(a) and 1(b) illustrate the bilayer-Na_3Bi/graphene heterostructure in top and side views, respectively. The optimized lattice parameters of bilayer Na_3Bi are $a =$

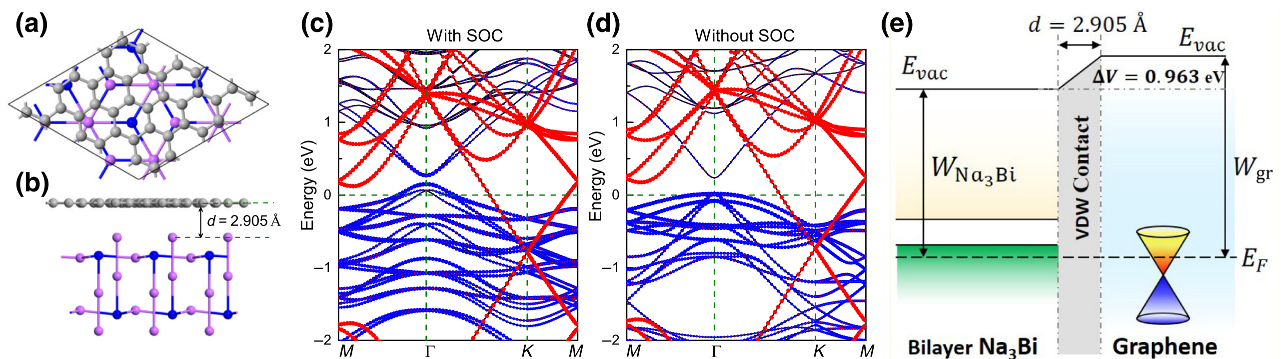

FIG. 1. (a) Top view and (b) side view of the bilayer-Na_3Bi/graphene heterostructure. (c),(d) Projected band structures with SOC and without SOC, respectively. The blue (red) dot projection originates from bilayer Na_3Bi (graphene). (e) Band alignments of the Na_3Bi/graphene heterostructure. ΔV represents the potential change generated by the interaction between graphene and bilayer Na_3Bi. The work functions of Na_3Bi and graphene are denoted as W_{Na_3Bi} and W_{gr}, respectively.

$b = 5.448$ Å, which agrees with the previously reported values [27], and the optimized lattice parameters of graphene are $a = b = 2.46$ Å. We consider a supercell with 2×2 and $\sqrt{19} \times \sqrt{19}$ periodicity for bilayer Na_3Bi and graphene, respectively. The lattice mismatch is 0.79%, and we stretch the graphene system while keeping the Na_3Bi lattice fixed so as to preserve the electronic properties of Na_3Bi. The energetically-most-stable configuration, depicted in Fig. 1(a), is obtained by our optimizing the lateral displacements of the graphene along the x and y directions with change of the vertical distance between bilayer Na_3Bi and graphene (see Fig. S1 in Supplemental Material [52]). The distance of the vdW gap is 2.905 Å at equilibrium.

The projected electronic band structure with and without SOC for the Na_3Bi/graphene heterostructure is shown in Figs. 1(c) and 1(d), respectively. The electronic band structures of both Na_3Bi and graphene are well preserved on formation of the heterostructure, while the band gap of bilayer Na_3Bi changes from 300 to 121 meV when SOC is included. Here graphene is n-doped because of the larger work function of graphene, which leads to the transfer of electrons from Na_3Bi to graphene. Such transfer also causes some of the valence band of Na_3Bi to cross the Fermi level [see Fig. 1(e) for the band alignments of bilayer-Na_3Bi/graphene contact]. Similar n-type doping was identified in a Cd_3As_2/graphene heterostructure [53], thus suggesting n-type doping is a common feature in ultrathin-Dirac-semimetal/graphene heterostructures. In contrast, dominant p-type doping has been reported in graphene contacted by bulk metals [54–56].

B. Bilayer-Na_3Bi/MoS_2 and bilayer-Na_3Bi/WS_2 heterostructures

We next study the contact between bilayer Na_3Bi and monolayers of MoS_2 and WS_2 (see Fig. 2). The Na_3Bi/MoS_2 and Na_3Bi/WS_2 heterostructures are constructed via stacking along the z direction. ForMoS_2 and WS_2, the lattice parameters are $a = b = 3.182$ Å and $a = b = 3.180$ Å, respectively. The $\sqrt{3} \times \sqrt{3}$ unit cells of MoS_2 and WS_2 are adjusted to match the 1×1 unit cell of bilayer Na_3Bi. The lattice mismatches are 0.77% and 0.73%, respectively. In Figs. 2(b)–2(d), we show the three possible stacking modes—namely, the AA, BB, and AB stacking configurations of Na_3Bi/MoS_2—as a representative example as the WS_2-based contact exhibits the same stacking structures. Here all S (yellow) [Mo (dark cyan)] atoms are above the Na (purple) and Bi (blue) atoms in the AA (BB) case and all atoms of Na_3Bi lie directly over the center of a hexagon in the upper MoS_2 (or WS_2) sheet in the AB case. The total energy of the Na_3Bi/MoS_2 and Na_3Bi/WS_2 heterostructures for different interlayer distances is shown in Fig. S2 in Supplemental Material [52]. After structural relaxation, we find

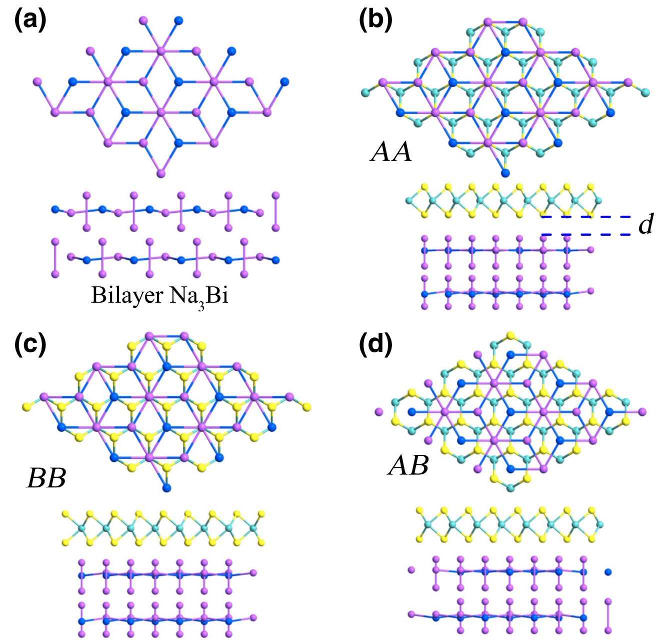

FIG. 2. (a) Top view (top panel) and side view (bottom panel) of the optimized structural geometry of bilayer Na_3Bi. (b)–(d) Same as (a) but with different stacking configurations for Na_3Bi/MoS_2 and Na_3Bi/WS_2. d is the interlayer distance.

that the different stacking modes exhibit various interlayer distances (see Table I). As the interlayer distances are close to the sum of the covalent radii of Na and S atoms, covalent bonds are expected to form between the two layers. To examine the energetic stability of Na_3Bi/MoS_2 and Na_3Bi/WS_2 electrical contacts, the binding energy E_b is calculated as $E_b = E_{Na_3Bi/MoS_2\,(WS_2)} - E_{Na_3Bi} - E_{MoS_2\,(WS_2)}$, where $E_{Na_3Bi/MoS_2\,(WS_2)}$ represents the total energy of the heterostructure and E_{Na_3Bi} and $E_{MoS_2\,(WS_2)}$ represent the energy of the isolated Na_3Bi and MoS_2 (WS_2), respectively. The calculated binding energies have negative values, thus indicating that the structures considered in our simulations are energetically stable. The calculated heterostructure parameters are summarized in Table I.

The band structures of an isolated Na_3Bi bilayer and a $\sqrt{3} \times \sqrt{3}$ MoS_2 (WS_2) monolayer are shown in Figs. 3(a)–3(c). Bilayer Na_3Bi exhibits a direct band gap of 0.1 eV at the Γ point, which is consistent with previous results [40]. The band gap is 1.73 eV for MoS_2 and 1.6 eV for WS_2, which are slightly less than the values reported in previous studies due to the presence of strain in the heterostructures considered here [57]. The projected band structures of the electrical contacts are shown in Figs. 3(d)–3(i) (see Fig. S3 in Supplemental Material [52] for the projected band structures without SOC). Here red, blue, and violet symbols denote the contributions from Na_3Bi, MoS_2, and WS_2, respectively. Compared with the band structures of isolated bilayer Na_3Bi, $\sqrt{3} \times \sqrt{3}$ MoS_2,

TABLE I. Calculated parameters of the Na_3Bi/2D-semiconductor heterostructures. d is the interlayer distance, d_a is the minimum distance between Na and S atoms, E_b is the binding energy, $E_{g(N)}$ and $E_{g(S)}$ are the band gap for Na_3Bi and MoS_2 or WS_2 after contact, respectively, D is the dipole moment, and W is the work function of the system.

	Na_3Bi/MoS_2			Na_3Bi/WS_2		
Stacking	*AA*	*BB*	*AB*	*AA*	*BB*	*AB*
d (Å)	2.665	2.186	2.198	2.696	2.257	2.269
d_a (Å)	2.665	2.84	2.85	2.696	2.90	2.90
E_b (eV)	−3.667	−3.831	−3.827	−3.543	−3.673	−3.668
$E_{g(N)}$ (eV)	0.131	0.274	0.278	0.116	0.279	0.249
$E_{g(S)}$ (eV)	1.701	1.653	1.709	1.558	1.547	1.522
D (D)	1.063	1.091	1.099	0.873	0.929	0.919
W (eV)	4.236	4.265	4.310	3.975	4.005	4.001

and WS_2 [Figs. 3(a)–3(c)], the band structures of Na_3Bi are not only up-shifted and show metallic behavior but also exhibit obvious band splitting. Strong splitting of the valence band around −0.5 eV at the Γ point is observed, which originates from the interactions between bilayer Na_3Bi and 2D TMDCs when they are forming the heterostructure. The valence bands of both MoS_2 and WS_2 are energetically down-shifted.

The conduction-band minimum is shifted from the Γ point to the M point, and crosses the Fermi level, thus indicating the formation of an Ohmic contact across the vdW gap [see Figs. 3(g)–3(i)]. The Ohmic contact persists even in the case of ten-layer-Na_3Bi (approximately-5-nm) contacts to MoS_2 and WS_2 (see Fig. S4 in Supplemental Material in [52]). Such an Ohmic vertical interface is in stark contrast to the case of 2D TMDCs contacted by Au and Ag, where a Schottky barrier is formed across the vertical vdW gap [58–60], which impedes the efficiency of charge injection. For other bulk metal electrodes such as Sc, Ti, and Pt electrodes, the band structures of 2D TMDCs are metalized in the contact region [58–60]. This is again in contrast to the case of Na_3Bi contacts to 2D TMDCs, where the hybridization between the two materials is weak. The band structures of 2D TMDCs are retained without the formation of a Schottky barrier across the vertical contact interface. Such Ohmic nature of the Na_3Bi-contacted MoS_2 and WS_2 suggests that electrons can be more efficiently injected through the vertical interfaces—a favorable characteristic for electronics and optoelectronics applications.

To further understand the detailed nature of the charge transfer at the Na_3Bi and MoS_2 and WS_2 interfaces, we calculate the charge difference between the combined heterostructure system and the sum of the isolated Na_3Bi and MoS_2 or WS_2 [see Figs. 4(a) and 4(c)]. The charge-density difference is calculated as $\Delta\rho = \rho_H - \rho_{Na_3Bi} - \rho_{MoS_2\,(WS_2)}$, where ρ_H, ρ_{Na_3Bi}, and $\rho_{MoS_2\,(WS_2)}$ are the charge density of the heterostructure, freestanding bilayer Na_3Bi, and isolated MoS_2 (WS_2), respectively. The blue regions represent electron depletion, while the red regions represent the accumulation of electrons in the heterostructures relative to their two isolated components. In the interfacial region, several charge-transfer oscillations are observed. The main charge depletion is contributed by the first layer of Na_3Bi closest to MoS_2

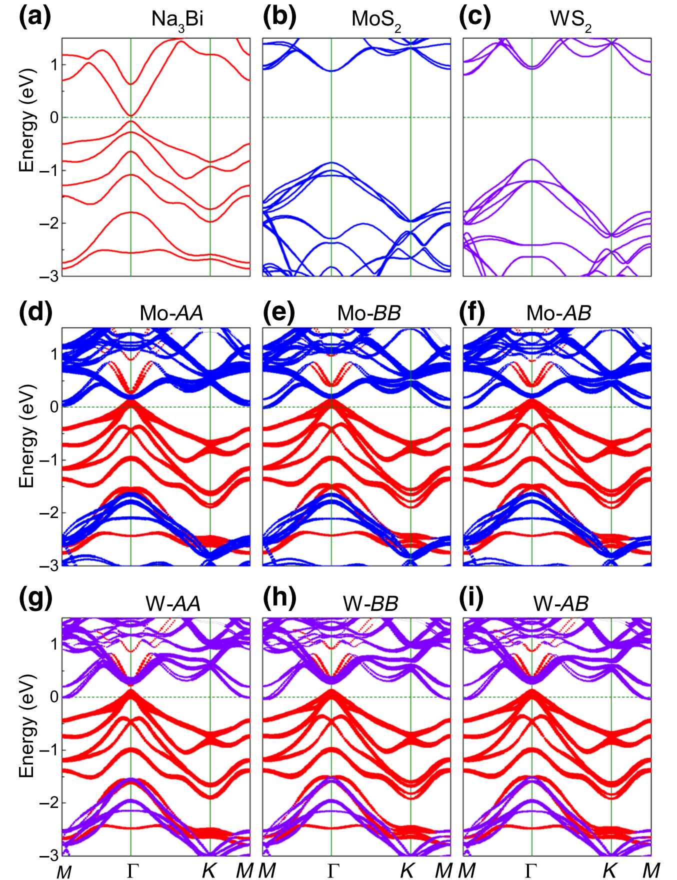

FIG. 3. Band structures of bilayer Na_3Bi (a), $\sqrt{3}\times\sqrt{3}$ MoS_2 (b), and $\sqrt{3}\times\sqrt{3}$ WS_2 (c). (d)–(f) Projected band structures of the heterostructure with SOC for Na_3Bi/MoS_2 with different stackings. (g)–(i) Projected band structures of the heterostructure with SOC for Na_3Bi/WS_2 with different stackings.

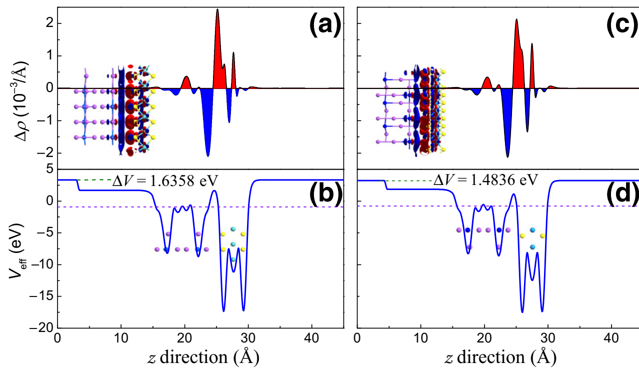

FIG. 4. Plane-averaged differential charge density $\Delta\rho$ and electrostatic potentials of Na_3Bi with (a),(b) MoS_2 and (c),(d) WS_2 heterostructure at equilibrium along the z direction. The insets show side views of the isosurfaces of the differential charge density of the heterostructure. ΔV reflects the difference between the work function on the Na_3Bi side and on the 2D-semiconductor side.

or WS_2. Moreover, some extra charge is found to accumulate around the Mo and W atoms. Compared with metal/MoS_2 and metal/WS_2 contacts, the major difference is the charge accumulation located in the MoS_2 or WS_2 interface [57,58]. In general, both the charge depletion and the charge accumulation constitute the interfacial charge-redistribution behavior, leading to electron-wave-function polarization and, hence, the formation of an interfacial electric dipole. The presence of such an interfacial dipole directly modifies the interfacial band alignment [61], thus leading to the band-structure modification shown in Figs. 3(d)–3(i).

To illustrate the key strengths of ultrathin Na_3Bi as an electrical contact to 2D TMDCs over other bulk metals, we simulate a field-effect-transistor device with 5-nm channel length [see Fig. 5(a)]. We use a nonequilibrium Green's function approach [52] to extract the height of the Schottky barrier laterally extending into the 2D channel by calculating the local device density of states, which reflects the energy-band distribution in real space along the simulated device [62,63]. The lateral electron Schottky-barrier height($\Phi^e_{L,T}$) of the MoS_2 and WS_2 transistors is estimated as the energy difference between the Fermi level, E_F, and the conduction-band minimum of the 2D channel [labeled in Figs. 5(b) and 5(c)]. $\Phi^e_{L,T}$ is calculated to be 0.32 and 0.18 eV, respectively, for MoS_2 and WS_2 [Figs. 5(b) and 5(c)], values which are appreciably lower than those of many other commonly studied bulk metals [59,60] because of the low work function of bilayer Na_3Bi (2.44 eV). In Fig. 6, $\Phi^e_{L,T}$ is plotted versus the isolated-metal work function (W_M) with use of the data for WS_2 and MoS_2 5-nm field-effect transistors extracted from Refs. [59,60]. Here $\Phi^e_{L,T}$ of bilayer Na_3Bi is substantially lower than that of other bulk metals. Particularly for WS_2 contacted

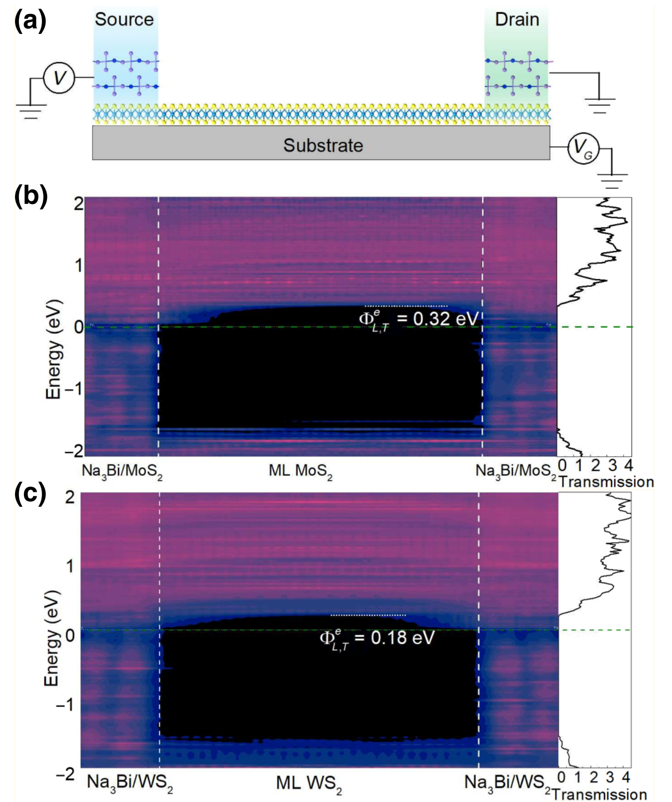

FIG. 5. (a) A 2D-TMDC field-effect transistor. (b),(c) Local device density of states (left panels) and transmission spectra (right panels) of MoS_2 and WS_2 transistors with Na_3Bi electrodes at zero gate and bias voltages. The horizontal green line represents the Fermi level. ML, monolayer.

by bilayer Na_3Bi , $\Phi^e_{L,T}$ is the lower than for other common bulk metal electrodes (i.e., Sc, Ti, Ag, Cu, Pd, and Pt electrodes) [60]. The relatively low $\Phi^e_{L,T}$ thus reveals the potential of bilayer Na_3Bi as another candidate electrode material to achieve high-efficiency charge injection into 2D TMDCs. We further remark that the pronounced Stark effect in Na_3Bi ultrathin film allows the band gap to be tuned and closed and the electronic band structure to be switched between a trivial band insulator and a topological insulator by an external gate voltage [40,41]. Such a gate-tunable metallic-insulator transition and topological phase transitions may offer a physical mechanism for the design of functional devices that is not found in conventional metal-semiconductor contacts and that is worthy of further exploration.

Finally, we remark that Na_3Bi is prone to degradation under ambient air conditions. Nonetheless, recent experiments [40] have successfully used angle-resolved photoemission spectroscopy and scanning tunneling microscopy to study the field-effect-tunable band structure in Na_3Bi, revealing a major step toward the fabrication of a Na_3Bi device. More recently, Na_3Bi ultrathin film passivated by

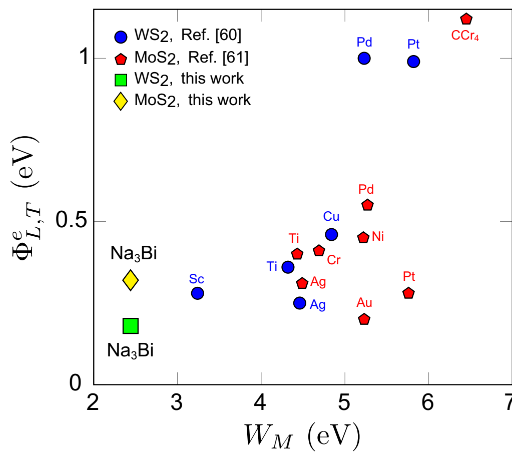

FIG. 6. Lateral Schottky-barrier height ($\Phi^e_{L,T}$) as a function of isolated-metal work function (W_M) for WS_2 [59] and MoS_2 [60].

MgF_2 or Si capping layers was demonstrated to be stable in air and the transport properties remained intact after such passivations [64]. Encapsulated Na_3Bi devices thus provide a potential route toward air-stable hybrid Na_3Bi/2D-semiconductor devices.

IV. CONCLUSION

In summary, we investigate the electronic and transport properties of the ultrathin topological Dirac semimetal Na_3Bi as an electrical contact to graphene, MoS_2, and WS_2 via first-principles calculations. We show that the Na_3Bi/graphene contact leads to n-type doping in graphene, which can be useful for electronics and optoelectronics applications, such as a p-n junction and a photodetector. For Na_3Bi/MoS_2 and Na_3Bi/WS_2, the prevalence of an Ohmic vertical interface and a low lateral Schottky-barrier height indicates the potential of Na_3Bi as an energy-efficient electrical contact. The findings reported here could ve a harbinger for the exploration of an emerging class of heterostructure electronic devices [65] that synergize 2D materials and the ever-expanding family of topological semimetals where nodal point, line, link, chain, double-helix, hourglass, surface, and many other exotic topological phases are continually being unearthed.

ACKNOWLEDGMENTS

This project is funded by Singapore MOE Tier 2 Grant (2018-T2-1-007) and USA ONRG grant (N62909-19-1-2047). LC acknowledge the support of Science Foundation of Hengyang Normal University of China (Grant No. 18D26), and the National Natural Science Foundation of China (Grants No. 11774085 and No. 11274108). GZ acknowledge the support of Hunan Provincial Natural Science Foundation of China (Grant No. 2019JJ50016). All calculations were performed with the computational resources provided by the National Supercomputing Centre Singapore.

[1] A. K. Geim and K. S. Novoselov, The rise of graphene, Nat. Mater. **6**, 183 (2007).
[2] S. Manzeli, D. Ovchinnikov, D. Pasquier, O. V. Yazyev, and A. Kis, 2D transition metal dichalcogenides, Nat. Rev. Mater. **2**, 17033 (2017).
[3] F. Xia, H. Wang, J. C. M. Hwang, A. H. Castro, and L. Yang, Black phosphorus and its isoelectronic materials, Nat. Rev. Phys. **1**, 306 (2019).
[4] A. Molle, J. Goldberger, M. Houssa, Y. Xu, S.-C. Zhang, and D. Akinwande, Buckled two-dimensional xene sheets, Nat. Mater. **16**, 163 (2017).
[5] M. Naguib, V. N. Mochalin, M. W. Baroum, and Y. Gogotsi, 25th anniversary article: MXenes: A new family of two-dimensional materials, Adv. Mater. **26**, 992 (2014).
[6] C. Gong, L. Li, Z. Li, H. Ji, A. Stern, Y. Xia, T. Cao, W. Bao, C. Wang, Y. Wang, Z. Q. Qiu, R. J. Cava, S. G. Louie, J. Xia, and X. Zhang, Discovery of intrinsic ferromagnetism in two-dimensional van der Waals crystals, Nature **546**, 265 (2017).
[7] Y. Deng, Y. Yu, Y. Song, J. Zhang, N. Z. Wang, Z. Sun, Y. Yi, Y. Z. Wu, S. Wu, J. Zhu, J. Wang, X. H. Chen, and Y. Zhang, Gate-tunable room-temperature ferromagnetism in two-dimensional Fe_3GeTe_2, Nature **563**, 94 (2018).
[8] G. Fiori, F. Bonaccorso, G. Iannaccone, T. Palacios, D. Neumaier, A. Seabaugh, S. K. Banerjee, and L. Colombo, Electronics based on two-dimensional materials, Nat. Nanotechnol. **9**, 768 (2014).
[9] F. Xia, H. Wang, D. Xiao, M. Dubey, and A. Ramasubramaniam, Two-dimensional material nanophotonics, Nat. Photonics **8**, 899 (2014).
[10] Q. H. Wang, K. Kalantar-Zadeh, A. Kis, J. N. Coleman, and M. S. Strano, Electronics and optoelectronics of two-dimensional transition metal dichalcogenides, Nat. Nanotechnol. **7**, 699 (2012).
[11] E. Pomerantseva and Y. Gogotsi, Two-dimensional heterostructures for energy storage, Nat. Energy **2**, 17089 (2017).
[12] S. Roche, J. Åkerman, B. Beschoten, J.-C. Charlier, M. Chshiev, S. P. Dash, B. Dlubak, J. Fabian, A. Fert, M. Guimarães, F. Guinea, I. Grigorieva, C. Schönenberger, P. Seneor, C. Stampfer, S. O. Valenzuela, X. Waintal, and B. van Wees, Graphene spintronics: The European flagship perspective, 2D Mater. **2**, 030202 (2015).
[13] J. R. Schaibley, H. Yu, G. Clark, P. Rivera, J. S. Ross, K. L. Seyler, W. Yao, and X. Xu, Valleytronics in 2D materials, Nat. Rev. Mater. **1**, 16055 (2016).
[14] Y. S. Ang, S. A. Yang, C. Zhang, Z. Ma, and L. K. Ang, Valleytronics in merging Dirac cones: All-electric-controlled valley filter, valve, and universal reversible logic gate, Phys. Rev. B **96**, 245410 (2017).
[15] A. Allain, J. H. Kang, K. Banerjee, and A. Kis, Electrical contacts to two-dimensional semiconductors, Nat. Mater. **14**, 1195 (2015).

[16] I. Popov, G. Seifeit, and D. Tománek, Designing Electrical Contacts to MoS_2 Monolayer: A Computational Study, Phys. Rev. Lett. **108**, 156802 (2012).

[17] X. Cui, G.-H. Lee, Y. D. Kim, G. Arefe, P. Y. Huang, C.-H. Lee, D. A. Chenet, X. Zhang, L. Wang, F. Ye, F. Pizzocchero, B. S. Jessen, K. Watanabe, T. Taniguchi, D. A. Muller, T. Low, P. Kim, and J. Hone, Multi-terminal transport measurements of MoS_2 using a van der Waals heterostructure device platform, Nat. Nanotechnol. **10**, 534 (2015).

[18] J. H. Kang, W. Liu, D. Sarkar, D. Jena, and K. Banerjee, Computational Study of Metal Contacts to Monolayer Transistion-Metal Dichalcogenide Semiconductors, Phys. Rev. X **4**, 031005 (2014).

[19] Y. S. Ang, H. Y. Yang, and L. K. Ang, Universal Scaling Laws in Schottky Heterostructures Based on Two-Dimensional Materials, Phys. Rev. Lett. **121**, 056802 (2018).

[20] Y. S. Ang, Y. Chen, C. Tan, and L. K. Ang, Generalized High-Energy Thermionic Electron Injection at Graphene Interface, Phys. Rev. Appl. **12**, 014057 (2019).

[21] Q. Y. Wu, Y. S. Ang, L. M. Cao, and L. K. Ang, Design of metal contacts for monolayer Fe_3GeTe_2 based devices, Appl. Phys. Lett. **115**, 083105 (2019).

[22] N. Briggs *et al.*, A roadmap for electronic grade 2D materials, 2D Mater. **6**, 022001 (2019).

[23] A. C. Ferrari *et al.*, Science and technology roadmap for graphene, related two-dimensional crystals, and hybrid systems, Nanoscale **7**, 4598 (2015).

[24] Z. K. Liu, B. Zhou, Y. Zhang, Z. J. Wang, H. M. Weng, D. Prabhakaran, S. K. Mo, Z. X. Shen, Z. Fang, X. Dai, Z. Hussain, and Y. L. Chen, Discovery of a three-dimensional topological Dirac semimetal, Na_3Bi, Science **343**, 864 (2014).

[25] S. Borisenko, Q. Gibson, D. Evtushinsky, V. Zabolotnyy, B. Bühner, and R. J. Cava, Experimental Realization of a Three-Dimensional Dirac Semimetal, Phys. Rev. Lett. **113**, 027603 (2014).

[26] M. Neupane, S.-Y. Xu, R. Sankar, N. Alidoust, G. Bian, C. Liu, I. Belopolski, T.-R. Chang, H.-T. Jeng, H. Lin, A. Bansil, F. C. Chou, and M. Z. Hasan, Observation of a three-dimensional topological Dirac semimetal phase in high-mobility Cd_3As_2, Nat. Commun. **5**, 3786 (2014).

[27] Z. J. Wang, Y. Sun, X. Q. Chen, C. Franchini, G. Xu, H. M. Weng, X. Dai, and Z. Fang, Dirac semimetal and topological phase transitions in A_3Bi ($A = Na, K, Rb$), Phys. Rev. B **85**, 195320 (2012).

[28] Z. J. Wang, H. M. Weng, Q. S. Wu, X. Dai, and Z. Fang, Three-dimensional Dirac semimetal and quantum transport in Cd_3As_2, Phys. Rev. B **88**, 125427 (2013).

[29] S. M. Young, S. Zaheer, J. C. Y. Teo, C. L. Kane, E. J. Mele, and A. M. Rappe, Dirac Semimetal in Three Dimensions, Phys. Rev. Lett. **108**, 140405 (2012).

[30] J. Xiong, S. K. Kushwaha, T. Liang, J. W. Krizan, M. Hirschberger, W. Wang, R. J. Cava, and N. P. Ong, Evidence for the chiral anomaly in the Dirac semimetal, Science **350**, 413 (2015).

[31] C. Zhang, E. Zhang, W. Wang, Y. Liu, Z.-G. Chen, S. Lu, S. Liang, J. Cao, X. Yuan, L. Tang, Q. Li, C. Zhou, T. Gu, Y. Wu, J. Zou, and F. Xiu, Room-temperature chiral charge pumping in Dirac semimetals, Nat. Commun. **8**, 13741 (2017).

[32] A. A. Abrikosov, Quantum magnetoresistance, Phys. Rev. B **58**, 2788 (1998).

[33] W. Zhang, R. Yu, W. Feng, Y. Yao, H. Weng, X. Dai, and Z. Fang, Topological Aspect and Quantum Magnetoresistance of β-Ag_2Te, Phys. Rev. Lett. **106**, 156808 (2011).

[34] C.-X. Liu, H. J. Zhang, B. Yan, X.-L. Qi, T. Frauenheim, X. Dai, Z. Fang, and S.-C. Zhang, Oscillatory crossover from two-dimensional to three-dimensional topological insulators, Phys. Rev. B **81**, 041307 (2010).

[35] J. Hellerstedt, M. T. Edmonds, N. Ramakrishnan, G. Liu, B. Weber, A. Tadich, K. M. O'Donnell, S. Adam, and M. S. Fuhrer, Electronic properties of high-quality epitaxial topological Dirac semimetal thin films, Nano Lett. **16**, 3210 (2016).

[36] P. Goswami and S. Chakravarty, Quantum Criticality between Topological and Band Insulators in $3 + 1$ Dimensions, Phys. Rev. Lett. **107**, 196803 (2011).

[37] M. Koshino and T. Ando, Anomalous orbital magnetism in Dirac-electron systems: Role of pseudospin paramagnetism, Phys. Rev. B **81**, 195431 (2010).

[38] X. Xiao, S. A. Yang, Z. Liu, H. Li, and G. Zhou, Anisotropic quantum confinement effect and electric control of surface states in Dirac semimetal nanostructures, Sci. Rep. **5**, 7898 (2015).

[39] K. J. A. Ooi, Y. S. Ang, Q. Zhai, D. T. H. Tan, L. K. Ang, and C. K. Ong, Nonlinear plasmonics of three-dimensional Dirac semimetals, APL Photonics **4**, 034402 (2019).

[40] J. L. Collins, A. Tadich, W. K. Wu, L. C. Gomes, J. N. B. Rodrigues, C. Liu, J. Hellerstedt, H. Ryu, S. J. Tang, S. K. Mo, S. Adam, S. A. Yang, M. S. Fuhrer, and M. T. Edmonds, Electric-field-tuned topological phase transition in ultrathin, Nature **564**, 390 (2018).

[41] H. Pan, M. Wu, Y. Liu, and S. A. Yang, Electric control of topological phase transitions in Dirac semimetal thin films, Sci. Rep. **5**, 14639 (2015).

[42] M. Eginligil, B. Cao, Z. Wang, X. Shen, C. Cong, J. Shang, C. Soci, and T. Yu, Dichroic spin-valley photocurrent in monolayer molybdenum disulphide, Nat. Commun. **6**, 7636 (2015).

[43] J. Lee, K. F. Mak, and J. Shan, Electrical control of the valley Hall effect in bilayer MoS_2 transistors, Nat. Nanotechnol. **11**, 421 (2016).

[44] G. Kresse and J. Furthmüller, Efficient iterative schemes for ab initio total-energy calculations using a plane-wave basis set, Phys. Rev. B **54**, 11169 (1996).

[45] G. Kresse and J. Furthmüller, Efficiency of ab-initio total energy calculations for metals and semiconductors using a plane-wave basis set, Comput. Mater. Sci. **6**, 15 (1996).

[46] G. Kresse and D. Joubert, From ultrasoft pseudopotentials to the projector augmented-wave method, Phys. Rev. B **59**, 1758 (1999).

[47] S. Grimme, J. Antony, S. Ehrlich, and H. Krieg, A consistent and accurate ab initio parametrization of density functional dispersion correction (DFT-D) for the 94 elements H-Pu, J. Chem. Phys. **132**, 154104 (2010).

[48] J. M. Soler, E. Artacho, J. D. Gale, A. García, J. Junquera, P. Ordejón, and D. Sáchez-Portal, The SIESTA method for

ab initio order-N materials simulation, J. Phys. Condens. Matter **14**, 2745 (2002).

[49] M. Brandbyge, J. L. Mozos, P. Ordejón, J. Taylor, and K. Stokbro, Density-functional method for nonequilibrium electron transport, Phys. Rev. B **65**, 165401 (2002).

[50] J. Taylor, H. Guo, and J. Wang, Ab initio modeling of quantum transport properties of molecular electronic devices, Phys. Rev. B **63**, 245407 (2001).

[51] J. Taylor, H. Guo, and J. Wang, Ab initio modeling of open systems: Charge transfer, electron conduction, and molecular switching of a C60 device, Phys. Rev. B **63**, 121104 (2001).

[52] See Supplemental Material http://link.aps.org/supplemental/10.1103/PhysRevApplied.13.054030 for the total energies of bilayer Na_3Bi/graphene (Fig. S1), bilayer Na_3Bi/MoS_2, and bilayer Na_3Bi/MoS_2 (Fig. S2), the projected band structures of bilayer Na_3Bi/MoS_2 and bilayer Na_3Bi/MoS_2 without SOC (Fig. S3), and the projected band structures of ten-layer Na_3Bi/MoS_2 and ten-layer Na_3Bi/MoS_2 with SOC (Fig. S4).

[53] Y.-F. Wu, L. Zhang, C.-Z. Li, Z.-S. Zhang, S. Liu, Z.-M. Liao, and D. P. Yu, Dirac semimetal heterostructures: 3D Cd_3As_2 on 2D graphene, Adv. Mater. **30**, 1707547 (2018).

[54] G. Giovannetti, P. A. Khomyakov, G. Brocks, V. M. Karpan, J. van den Brink, and P. J. Kelly, Doping Graphene with Metal Contacts, Phys. Rev. Lett. **101**, 026803 (2008).

[55] P. A. Khomyakov, G. Giovannetti, P. C. Rusu, G. Brocks, J. van den Brink, and P. J. Kelly, First-principles study of the interaction and charge transfer between graphene and metals, Phys. Rev. B **79**, 195425 (2009).

[56] H. C. Diaz, R. Addoua, and M. Batzilla, Interface properties of CVD grown graphene transferred onto MoS_2(0001), Nanoscale **6**, 1071 (2014).

[57] W. Chen, E. J. G. Santos, W. G. Zhu, E. Kaxiras, and Z. Y. Zhang, Tuning the electronic and chemical properties of monolayer adsorbed on transition metal substrates, Nano Lett. **13**, 509 (2013).

[58] C. Gong, L. Colombo, R. M. Wallace, and K. Cho, The unusual mechanism of partial Fermi level pinning at metal-MoS_2 interfaces, Nano Lett. **14**, 1714 (2014).

[59] H. Tang, B. Shi, Y. Pan, J. Li X. Zhang, J. Yan, S. Liu, J. Yang, L. Xu, J. Yang, M. Wu, and J. Lu, Schottky contact in monolayer field-effect transistors, Adv. Theory Simul. **2**, 1900001 (2019).

[60] Y. Pan, J. Gu, H. Tang, X. Zhang, J. Li, B. Shi, J. Yang, H. Zhang, J. Yang, S. Liu, H. Hu, M. Wu, and J. Lu, Reexamination of the schottky barrier heights in monolayer field-effect transistors, ACS Appl. Nano Mater. **2**, 4717 (2019).

[61] R. T. Tung, Formation of an electric dipole at metal-semiconductor interfaces, Phys. Rev. B **64**, 205310 (2001).

[62] S. Das, W. Zhang, M. Demarteau, A. Hoffmann, M. Dubey, and A. Roelofs, Tuanble transport gap in phosphorene, Nano Lett. **14**, 5733 (2014).

[63] Y. Du, H. Liu, Y. Deng, and P. D. Ye, Device perspective for black phosphorus field-effect transistors: Contact resistance, ambipolar behavior, and scaling, ACS Nano **8**, 10035 (2014).

[64] C. Liu, G. Akhgar, J. L. Collins, J. Hellerstedt, S. Adam, M. S. Fuhrer, and M. T. Edmonds, Quantum transport in air-stable Na_3Bi thin films, arXiv:2003.13171 (2020).

[65] S.-J. Liang, B. Cheng, X. Cui, and F. Miao, Van der Waals heterostructures for high-performance device applications: Challenges and opportunities, Adv. Mater. 1903800 (2019).